

Density constrained TDHF*

V.E. Oberacker and A.S. Umar

Department of Physics and Astronomy, Vanderbilt University, Nashville, TN 37235, USA

E-mail: volker.e.oberacker@vanderbilt.edu, umar@compsci.cas.vanderbilt.edu

Abstract: In this manuscript we provide an outline of the numerical methods used in implementing the density constrained time-dependent Hartree-Fock (DC-TDHF) method and provide a few examples of its application to nuclear fusion. In this approach, dynamic microscopic calculations are carried out on a three-dimensional lattice and there are no adjustable parameters, the only input is the Skyrme effective NN interaction. After a review of the DC-TDHF theory and the numerical methods, we present results for heavy-ion potentials $V(R)$, coordinate-dependent mass parameters $M(R)$, and precompound excitation energies $E^*(R)$ for a variety of heavy-ion reactions. Using fusion barrier penetrabilities, we calculate total fusion cross sections $\sigma(E_{\text{c.m.}})$ for reactions between both stable and neutron-rich nuclei. We also determine capture cross sections for hot fusion reactions leading to the formation of superheavy elements.

keywords: TDHF, DC-TDHF, heavy-ion fusion, neutron-rich nuclei, superheavy elements

1 Introduction

The theoretical investigation of heavy-ion interaction potentials $V(R)$ is of fundamental importance for the study of fusion reactions at energies in the vicinity of the Coulomb barrier. Radioactive ion beam facilities enable us to study fusion reactions with exotic neutron-rich nuclei [1]. An important goal of these experiments is to study the effects of neutron excess ($N - Z$) on fusion. Another theoretical challenge is to provide guidance to fusion experiments leading to the formation of new superheavy elements. And finally, fusion of very neutron rich nuclei plays a major role in nuclear astrophysics where it determines the composition and heating of the crust of accreting neutron stars. A recent review of the state of heavy-ion fusion including the DC-TDHF method can be found in [2].

In the absence of a practical quantum many-body theory of barrier tunneling, sub-barrier fusion calculations are commonly performed in two steps; the calculation of a heavy-ion interaction potential $V(R)$ and a subsequent calculation of tunneling through the barrier. Theoretical studies of fusion cross sections are often done by employing phenomenological methods such as the coupled-channels approach [3, 4] in which one uses empirical ion-ion potentials or double-folding potentials calculated with “frozen density” approximation and low-lying excitations are incorporated using macroscopic models. These calculations ignore dynamical effects such as neck formation, particle exchange, pre-equilibrium GDR and other modes during the nuclear overlap phase of the reaction. During this phase of the collision the primary underlying mechanism is the dynamical change in the density along the fusion path which modifies the potential energy. Obviously, this density change is not instantaneous. For instance, it was shown in Ref. [5] that the development of a neck due to couplings to octupole phonons in $^{40}\text{Ca}+^{40}\text{Ca}$ could take approximately one zeptosecond. As a consequence, the dynamical change of the density is most significant at low energy (near the barrier-top) where the colliding partners spend enough time in the vicinity of each other with little relative kinetic energy. At high energies, however, the nuclei

* To be published as a commemorative ebook focusing on the field of nuclear reaction theory and on the work related to Prof. Joachim Maruhn.

overcome the barrier essentially in their ground-state density. This energy dependence of the effect of the couplings on the density evolution was clearly shown in TDHF calculations by Washiyama and Lacroix [6]. This naturally translates into an energy dependence of the nucleus-nucleus potential [7, 8], similar to what was introduced phenomenologically in the Sao-Paulo potential [9]. Consequently, the barrier corresponding to near barrier-top energies includes dynamical couplings effects and can be referred to as a *dynamic-adiabatic* barrier, while at high energy the nucleus-nucleus interaction is determined by a *sudden* potential which can be calculated assuming frozen ground-state densities.

We have developed a dynamic microscopic approach, the density constrained time-dependent Hartree-Fock (DC-TDHF) method [10], to calculate heavy-ion interaction potentials $V(R)$, mass parameters $M(R)$, and precompound excitation energies $E^*(R)$ [11] directly from microscopic TDHF dynamics. The idea of constraining the dynamical density during a TDHF collision to find the collective path corresponding to the dynamical changes of the nuclear density was first introduced in a collaborative work of Prof. Maruhn in 1985 [12]. This novel approach has facilitated the present calculations of sub-barrier fusion cross sections, capture cross sections for superheavy element production, and nuclear astrophysics applications. The theory has been applied to calculate fusion cross-sections for the fusion of light to heavy systems [7, 13–21]. In this paper we will summarize the DC-TDHF method and outline the numerical algorithms involved in solving the static and dynamic equations of motion. For a variety of heavy-ion reactions, we discuss numerical calculations of fusion / capture cross-sections and compare these to experimental data if available.

2 Theoretical formalism

The theoretical formalism for the microscopic description of complex many-body quantum systems and the understanding of the nuclear interactions that result in self-bound, composite nuclei possessing the observed properties are the underlying challenges for studying low energy nuclear physics. The Hartree-Fock approximation and its time-dependent generalization, the time-dependent Hartree-Fock theory, has provided a possible means to study the diverse phenomena observed in low energy nuclear physics including collective vibrations [22–25] and nuclear reactions [26, 27].

2.1 Time-dependent Hartree-Fock (TDHF) method

Given a many-body Hamiltonian containing two and three-body interactions

$$H = \sum_i^N t_i + \sum_{i<j}^N v_{ij} + \sum_{i<j<k}^N v_{ijk} , \quad (1)$$

the time-dependent action S can be constructed as

$$S = \int_{t_1}^{t_2} dt \langle \Phi(t) | H - i\hbar\partial_t | \Phi(t) \rangle . \quad (2)$$

Here, Φ denotes the time-dependent, many-body wavefunction, $\Phi(\mathbf{r}_1, \mathbf{r}_2, \dots, \mathbf{r}_A; t)$, and t_i is the one-body kinetic energy operator. General variation of S recovers the time-dependent Schrödinger equation. In TDHF approximation the many-body wavefunction is replaced by a single Slater determinant and this form is preserved at all times. The determinantal form guarantees the antisymmetry required by the Pauli principle for a system of fermions. In this limit, the variation of the action yields the most probable time-dependent path between points t_1 and t_2 in the multi-dimensional space-time phase space

$$\delta S = 0 \rightarrow \Phi(t) = \Phi_0(t) . \quad (3)$$

In practice $\Phi_0(t)$ is chosen to be a Slater determinant

$$\Phi_0(t) = \frac{1}{\sqrt{N!}} \det |\phi_\lambda(\mathbf{r}, t)| , \quad (4)$$

where $\phi_\lambda(\mathbf{r}, t)$ are the single-particle states with quantum numbers λ . If the variation in Eq.(3) is performed with respect to the single-particle states ϕ_λ^* we obtain a set of coupled, nonlinear, self-consistent initial value equations for the single-particle states

$$h(\{\phi_\mu\})\phi_\lambda = i\hbar\dot{\phi}_\lambda \quad \lambda = 1, \dots, N. \quad (5)$$

These are the fully microscopic time-dependent Hartree-Fock equations which preserve the major conservation laws such as the particle number, total energy, total angular momentum, etc. As we see from Eq.(5), each single-particle state evolves in the mean-field generated by the concerted action of all the other single-particle states. Static equations can be obtained from Eq.(5) by taking out a trivial phase from the single-particle states

$$\begin{aligned} h(\{\chi_\mu\})\chi_\lambda &= \epsilon_\lambda\chi_\lambda \\ \phi_\lambda(\mathbf{r}, t) &= e^{-i\epsilon_\lambda t/\hbar}\chi_\lambda(\mathbf{r}). \end{aligned} \quad (6)$$

In TDHF, the initial nuclei are calculated using the static Hartree-Fock (HF) theory. The resulting Slater determinants for each nucleus comprise the larger Slater determinant describing the colliding system during the TDHF evolution. Nuclei are assumed to move on a pure Coulomb trajectory until the initial separation between the nuclear centers used in TDHF evolution. Using the Coulomb trajectory we compute the relative kinetic energy at this separation and the associated translational momenta for each nucleus. The nuclei are then boosted by multiplying the HF states with

$$\Phi_j \rightarrow \exp(i\mathbf{k}_j \cdot \mathbf{R})\Phi_j, \quad (7)$$

where Φ_j is the HF state for nucleus j and \mathbf{R} is the corresponding center of mass coordinate

$$\mathbf{R} = \frac{1}{A_j} \sum_{i=1}^{A_j} \mathbf{r}_i. \quad (8)$$

The Galilean invariance of the TDHF equations assures the evolution of the system without spreading and the conservation of the total energy for the system. In TDHF, the many-body state remains a Slater determinant at all times. The final state is a filled determinant, even in the case of two well separated fragments. This phenomenon is commonly known as the ‘‘cross-channel coupling’’ and indicates that it is not possible to identify the well separated fragments as distinct nuclei since each single particle state will have components distributed everywhere in the numerical box [28]. In this sense it is only possible to extract *inclusive* (averaged over all states) information from these calculations.

2.2 DC-TDHF method

The concept of using density as a constraint for calculating collective states from TDHF time-evolution was first introduced in Ref. [12], and used in calculating collective energy surfaces in connection with nuclear molecular resonances in Ref. [29].

In this approach we assume that a collective state is characterized only by density ρ , and current \mathbf{j} . This state can be constructed by solving the static Hartree-Fock equations

$$\langle \Phi_{\rho,\mathbf{j}} | a_h^\dagger a_p \hat{H} | \Phi_{\rho,\mathbf{j}} \rangle = 0, \quad (9)$$

subject to constraints on density and current

$$\begin{aligned} \langle \Phi_{\rho,\mathbf{j}} | \hat{\rho}(\mathbf{r}) | \Phi_{\rho,\mathbf{j}} \rangle &= \rho(\mathbf{r}, t) \\ \langle \Phi_{\rho,\mathbf{j}} | \hat{\mathbf{j}}(\mathbf{r}) | \Phi_{\rho,\mathbf{j}} \rangle &= \mathbf{j}(\mathbf{r}, t). \end{aligned}$$

Choosing $\rho(\mathbf{r}, t)$ and $\mathbf{j}(\mathbf{r}, t)$ to be the instantaneous TDHF density and current results in the lowest energy collective state corresponding to the instantaneous TDHF state $|\Phi(t)\rangle$, with the corresponding energy

$$E_{coll}(\rho(t), \mathbf{j}(t)) = \langle \Phi_{\rho,\mathbf{j}} | \hat{H} | \Phi_{\rho,\mathbf{j}} \rangle. \quad (10)$$

This collective energy differs from the conserved TDHF energy only by the amount of internal excitation present in the TDHF state, namely

$$E^*(t) = E_{TDHF} - E_{coll}(t). \quad (11)$$

However, in practical calculations the constraint on the current is difficult to implement but we can define instead a static adiabatic collective state $|\Phi_\rho\rangle$ subject to the constraints

$$\begin{aligned} \langle \Phi_\rho | \hat{\rho}(\mathbf{r}) | \Phi_\rho \rangle &= \rho(\mathbf{r}, t) \\ \langle \Phi_\rho | \hat{j}(\mathbf{r}) | \Phi_\rho \rangle &= 0. \end{aligned}$$

In terms of this state one can write the collective energy as

$$E_{coll} = E_{kin}(\rho(t), \mathbf{j}(t)) + E_{DC}(\rho(\mathbf{r}, t)), \quad (12)$$

where the density constrained energy E_{DC} , and the collective kinetic energy E_{kin} are defined as

$$\begin{aligned} E_{DC} &= \langle \Phi_\rho | \hat{H} | \Phi_\rho \rangle \\ E_{kin} &\approx \frac{\hbar^2}{2m} \sum_q \int d^3r \mathbf{j}_q(t)^2 / \rho_q(t), \end{aligned}$$

where the index q is the isospin index for neutrons and protons ($q = n, p$).

2.3 DC-TDHF applications: ion-ion potential, mass parameter, and precompound excitation energy

Recently, we have developed a new method to extract ion-ion interaction potentials directly from the TDHF time-evolution of the nuclear system [10]. In the DC-TDHF approach the TDHF time-evolution takes place with no restrictions. At certain times t or, equivalently, at certain internuclear distances $\bar{R}(t)$ the instantaneous TDHF density is used to perform a static DFT energy minimization while constraining the proton and neutron densities to be equal to the instantaneous TDHF densities. This means we allow the single-particle wave functions to rearrange themselves in such a way that the total energy is minimized, subject to the TDHF density constraint. In a typical DC-TDHF run, we utilize a few thousand time steps, and the density constraint is applied every 10 – 20 time steps.

In essence, DC-TDHF provides us with the TDHF dynamical path in relation to the multi-dimensional static energy surface of the combined nuclear system. In this approach there is no need to introduce constraining operators which assume that the collective motion is confined to the constrained phase space. In short, we have a self-organizing system which selects its evolutionary path by itself following the microscopic dynamics.

We refer to the minimized energy as the “density constrained energy” E_{DC} . From Eq. 12 it is clear that the density constrained energy plays the role of a collective potential, except for the fact that it contains the binding energies of the two colliding nuclei. One can thus define the ion-ion potential as [10]

$$V(\bar{R}(t)) = E_{DC}(\rho(\mathbf{r}, t)) - E_{A_1} - E_{A_2}, \quad (13)$$

where E_{A_1} and E_{A_2} are the binding energies of two nuclei obtained from a static Hartree-Fock calculation with the same effective interaction. For describing a collision of two nuclei one can label the above potential with ion-ion separation distance $\bar{R}(t)$ obtained during the TDHF time-evolution. This ion-ion potential $V(\bar{R})$ is asymptotically correct since at large initial separations it exactly reproduces $V_{Coulomb}(\bar{R}_{max})$. All of the dynamical features included in TDHF are naturally included in the DC-TDHF potentials. These effects include neck formation, particle exchange [30–32], internal excitations, and deformation effects to all order, among others. Couplings between relative motion and internal structures are known to affect fusion barriers by dynamically modifying the densities of the colliding nuclei. The

effect is expected to be stronger at energies near the barrier top, where changes in density have longer time to develop than at higher energies. This gives rise to an energy dependence of the barriers as predicted by modern time-dependent Hartree-Fock (TDHF) calculations [5–7].

The TDHF evolution also provides us with a coordinate-dependent mass $M(\bar{R})$ which may be obtained using energy conservation for a central collision

$$M(\bar{R}) = \frac{2[E_{\text{c.m.}} - V(\bar{R})]}{\dot{\bar{R}}^2}, \quad (14)$$

where the collective velocity $\dot{\bar{R}}$ is directly obtained from the TDHF evolution. The \bar{R} -dependence of this mass at lower energies is very similar to the one found in constrained Hartree-Fock calculations [33] with a constraint on the quadrupole moment. On the other hand, at higher energies the coordinate dependent mass essentially becomes flat, which is again a sign that most dynamical effects are contained at lower energies. The peak at small \bar{R} values is due to the fact that the center-of-mass energy is above the barrier and the denominator of Eq. (14) becomes small due to the slowdown of the ions.

The fusion barrier penetrabilities $T_L(E_{\text{c.m.}})$ can be obtained by numerical integration of the Schrödinger equation for the collective distance coordinate \bar{R} , using the heavy-ion potential $V(\bar{R})$ with coordinate dependent mass parameter $M(\bar{R})$. Alternatively, we can instead use the constant reduced mass μ and transfer the coordinate-dependence of the mass to a scaled potential $V(R)$ using the well known exact point transformation [17, 33]

$$dR = \left(\frac{M(\bar{R})}{\mu} \right)^{\frac{1}{2}} d\bar{R}. \quad (15)$$

The potential $V(R)$, which includes the coordinate-dependent mass effects differs from the $V(\bar{R})$ only in the interior region of the barrier. Further details can be found in Ref. [17].

The fusion barrier penetrabilities $T_L(E_{\text{c.m.}})$ are obtained by numerical integration of the Schrödinger equation

$$\left[\frac{-\hbar^2}{2\mu} \frac{d^2}{dR^2} + \frac{L(L+1)\hbar^2}{2\mu R^2} + V(R) - E_{\text{c.m.}} \right] \psi(R) = 0, \quad (16)$$

using the *incoming wave boundary condition* (IWBC) method [34]. IWBC assumes that once the minimum of the potential is reached fusion will occur. In practice, the Schrödinger equation is integrated from the potential minimum, R_{min} , where only an incoming wave is assumed, to a large asymptotic distance, where it is matched to incoming and outgoing Coulomb wavefunctions. The barrier penetration factor, $T_L(E_{\text{c.m.}})$, is the ratio of the incoming flux at R_{min} to the incoming Coulomb flux at large distance. Here, we implement the IWBC method exactly as it is formulated for the coupled-channel code CCFULL described in Ref. [35]. This gives us a consistent way for calculating cross-sections at energies below and above the barrier via

$$\sigma_f(E_{\text{c.m.}}) = \frac{\pi}{k^2} \sum_{L=0}^{\infty} (2L+1) T_L(E_{\text{c.m.}}). \quad (17)$$

At energies above the barrier either the DC-TDHF method or direct TDHF calculations can be used to determine the fusion cross-sections. The precompound excitation energy $E^*(R(t))$ can be computed from Eq. 11.

The DC-TDHF calculations mentioned above utilize the potential $V(R)$, which includes the coordinate-dependent mass effects, to find the cross-sections using Eq. 16. Recently, a systematic study was performed to calculate the potential and coordinate dependent mass for non-central TDHF collisions [8].

2.4 Skyrme interaction

Almost all TDHF calculations have been done using the Skyrme energy density functional. The Skyrme energy density functional contains terms which depend on the nuclear

density, ρ , kinetic-energy density, τ , spin density, \mathbf{s} , spin kinetic energy density, \mathbf{T} , and the full spin-current pseudotensor, \mathbf{J} , as

$$E = \int d^3r \mathcal{H}(\rho, \tau, \mathbf{j}, \mathbf{s}, \mathbf{T}, \mathbf{J}; \mathbf{r}) . \quad (18)$$

The time-odd terms ($\mathbf{j}, \mathbf{s}, \mathbf{T}$) vanish for static calculations of even-even nuclei, while they are present for odd mass nuclei, in cranking calculations, as well as in TDHF. The spin-current pseudotensor, \mathbf{J} , is time-even and does not vanish for static calculations of even-even nuclei. It has been shown [36–41] that the presence of these extra terms are necessary for preserving the Galilean invariance and make an appreciable contribution to the dissipative properties of the collision. Our TDHF program includes all of the appropriate combinations of time-odd terms in the Skyrme interaction. In addition, commonly a pairing force is added to incorporate pairing interactions for nuclei. The implementation of pairing for time-dependent collisions is currently an unresolved problem although small amplitude implementations exist [42–44]. However, for reactions with relatively high excitation this is not expected to be a problem.

3 Numerical methods

In this section we discuss the numerical details of performing TDHF calculations of nuclear collisions as well as the density-constraint method, which is crucial for ion-ion potential calculations. Relatively recently it has become feasible, for the first time, to perform TDHF calculations on a 3D Cartesian grid without any symmetry restrictions and with much more accurate numerical methods [39, 45, 46]. At the same time the quality of effective interactions has also been substantially improved [47–50].

3.1 Discrete variation and lattice equations

The lattice solution of differential equations on a discretized mesh of independent variables may be viewed to proceed in two steps: (1) Obtain a discrete representation of the functions and operators on the lattice. (2) Solve the resulting lattice equations using iterative techniques. Step (1) is an interpolation problem for which we could take advantage of the techniques developed using the basis-spline functions [51, 52]. The use of the basis-spline collocation method leads to a matrix-vector representation on the collocation lattice with a metric describing the transformation properties of the collocation lattice.

In order to obtain a set of lattice equations which preserve the conservation laws associated with the continuous equations it is essential to develop a modified variational approach. This goal is achieved by performing a variation to the discretized form of a conserved quantity, i.e. total energy. Consequently, the resulting equations will preserve all of the conserved quantities on the lattice. For the TDHF equations we consider a general discretized form of the action

$$S = \int dt \sum_{\alpha\beta\gamma} \Delta V_{\alpha\beta\gamma} \left\{ \mathcal{H}(\alpha\beta\gamma) - \left[i\hbar \sum_{\mu} \psi_{\mu}^*(\alpha\beta\gamma) \frac{\partial \psi_{\mu}}{\partial t}(\alpha\beta\gamma) \right] \right\} , \quad (19)$$

where indices α, β, γ denote the lattice points in three-dimensional space, and $\Delta V_{\alpha\beta\gamma}$ is the corresponding infinitesimal volume element. Due to the presence of derivative operators in the Hamiltonian the explicit form of these expressions will depend non-locally on the lattice indices. The general variation, which preserves the properties of the continuous variation, is given by

$$\frac{\delta \psi_{\mu}^*(\alpha\beta\gamma)}{\delta \psi_{\lambda}^*(\alpha'\beta'\gamma')} = \frac{1}{\Delta V_{\alpha\beta\gamma}} \delta_{\lambda\mu} \delta_{\alpha'\alpha} \delta_{\beta'\beta} \delta_{\gamma'\gamma} . \quad (20)$$

Until recently, most HF and TDHF calculations have been performed using finite-difference lattice techniques. The details of the discrete variation for the finite-difference case are given in Refs. [38, 53]. Below we outline a procedure for using the BSCM for the numerical solution of HF and TDHF equations. Further details of the BSCM is published elsewhere [51].

3.2 Basis-splines

Given a set of points or *knots* denoted by the set $\{x_i\}$ a basis-spline (B-spline denoted by B_i^M) function of order M is constructed from continuous piecewise polynomials of order $M - 1$ [54]. B-splines have continuous derivatives up to $(M - 2)^{nd}$ derivative and a discontinuous $(M - 1)^{st}$ derivative. We only consider odd order splines or even order polynomials for reasons related to the choice of the collocation points. The i^{th} B-spline is nonzero only in the interval (x_i, x_{i+M}) . This property is commonly referred to as limited support. The knots are the points where polynomials that make up the B-spline join. In the interval containing the tail region B-splines fall off very rapidly to zero. An example of order $M = 5$ splines extending over a physical region is illustrated in Fig.1. We can also construct exact derivatives of B-splines provided the derivative order does not exceed $M - 1$.

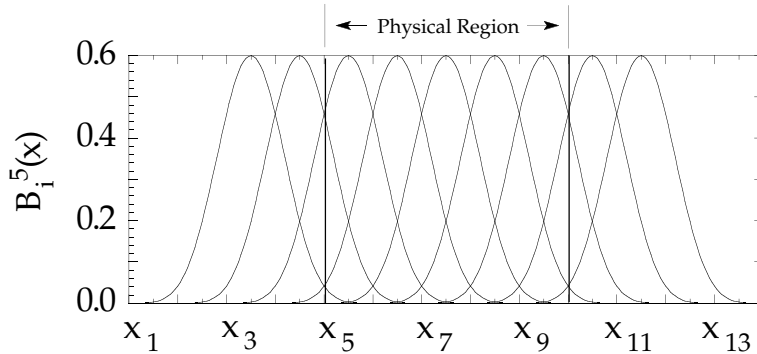


Figure 1: A region of space with physical boundaries located at knots x_M and x_{M+N} for $M = 5$ and $N = 5$. The B-spline B_1^M which begins at the first knot x_1 has its tail in the physical region. The last B-spline which begins within the physical boundaries is B_{N+M-1}^M . It extends up to the last knot x_{N+2M-1} .

A continuous function $f(x)$, defined in the interval (x_{min}, x_{max}) , can be expanded in terms of B-spline functions as

$$f(x) = \sum_i B_i^M(x) c^i, \quad (21)$$

where quantities c^i denote the expansion coefficients. We can solve for the expansion coefficients in terms of a given (or to be determined) set of function values evaluated at a set of data points more commonly known as *collocation points*. There are a number of ways to choose collocation points [51, 54], however, for odd order B-splines a simple choice is to place one collocation point at the center of each knot interval within the physical boundaries

$$x_\alpha = \frac{x_{\alpha+M-1} + x_{\alpha+M}}{2}, \quad \alpha = 1, \dots, N. \quad (22)$$

Here, $x_M = x_{min}$, $x_{N+M} = x_{max}$, and N is the number of collocation points. We can now write a linear system of equations by evaluating (21) at these collocation points

$$f_\alpha = \sum_i B_{\alpha i} c^i, \quad (23)$$

where $f_\alpha \equiv f(x_\alpha)$, and $B_{\alpha i} \equiv B_i^M(x_\alpha)$. In order to solve for the expansion coefficients the matrix \mathbf{B} needs to be inverted. However, as it stands matrix \mathbf{B} is not a square matrix, since the total number of B-splines with a nonzero extension in the physical region is $N + M - 1$. In order to perform the inversion we need to introduce additional linear equations which represent the boundary conditions imposed on $f(x)$ at the two boundary points, x_M and x_{M+N} . The essence of the lattice method is to eliminate the expansion coefficients c^i using this inverse matrix. The details of using the boundary conditions (or periodic boundaries)

and inverting the resulting square matrix are discussed in Ref. [51]. Following the inversion the coefficients are given by

$$c^i = \sum_{\alpha} [\mathbf{B}^{-1}]^{i\alpha} f_{\alpha} . \quad (24)$$

One can trivially show that all local functions will have a local representation in the finite dimensional collocation space

$$f(x) \longrightarrow f_{\alpha} . \quad (25)$$

The collocation representation of the operators can be obtained by considering the action of an operator \mathcal{O} onto a function $f(x)$

$$\mathcal{O}f(x) = \sum_i [\mathcal{O}B_i^M(x)] c^i . \quad (26)$$

If we evaluate the above expression at the collocation points x_{α} we can write

$$[\mathcal{O}f]_{\alpha} = \sum_i [\mathcal{O}B]_{\alpha i} c^i . \quad (27)$$

Substituting from Eq. (24) for the coefficients c^i we obtain

$$\begin{aligned} [\mathcal{O}f]_{\alpha} &= \sum_{i\beta} [\mathcal{O}B]_{\alpha i} [\mathbf{B}^{-1}]^{i\beta} f_{\beta} \\ &= \sum_{\beta} O_{\alpha}^{\beta} f_{\beta} , \end{aligned} \quad (28)$$

where we have defined the collocation space matrix representation of the operator \mathcal{O} by

$$O_{\alpha}^{\beta} = \sum_i [\mathcal{O}B]_{\alpha i} [\mathbf{B}^{-1}]^{i\beta} . \quad (29)$$

Notice that the construction of the collocation space operators can be performed once and for all at the beginning of a calculation, using only the given knot sequence and collocation points. Due to the presence of the inverse in Eq. (29) the matrix O is not sparse. In practice, operator \mathcal{O} is chosen to be a differential operator such as d/dx or d^2/dx^2 . By a similar construction it is also possible to obtain the appropriate integration weights on the collocation lattice [51].

3.3 Discrete HF equations

Since the detailed derivation of the BSCM representation of the TDHF equations involve many terms that are present in the energy functional, we will only show few terms. The three-dimensional expansion in terms of B-splines is a simple generalization of Eq. (21)

$$\psi_{\lambda}(x, y, z) = \sum_{ijk} c_{\lambda}^{ijk} B_i(x) B_j(y) B_k(z) . \quad (30)$$

The knots and collocation points for each coordinate can be different. With the appropriate definition of boundary conditions all of the discretization techniques discussed in the previous section can be generalized to the three-dimensional space. The details of this procedure are given in [51].

As an example for a local term let us consider a part of the t_0 contribution to the total energy

$$\frac{t_0}{2} \left(1 + \frac{x_0}{2}\right) \int d^3r \rho^2 = \frac{t_0}{2} \left(1 + \frac{x_0}{2}\right) \sum_{\alpha\beta\gamma} w^{\alpha} w^{\beta} w^{\gamma} [\rho(\alpha\beta\gamma)]^2 , \quad (31)$$

where on the right-hand side we have written the discretized form on a collocation lattice with collocation weights denoted by w . Here, α, β, γ represent the collocation points in $x, y,$

and z directions, respectively. In order to be able to perform the variation with respect to the single-particle states ψ_λ^* we rewrite equation (31) explicitly

$$\frac{t_0}{2} \left(1 + \frac{x_0}{2}\right) \sum_{\alpha\beta\gamma} w^\alpha w^\beta w^\gamma \sum_{\mu\nu} \psi_\mu^* \psi_\mu \psi_\nu^* \psi_\nu . \quad (32)$$

Using Eq.(20) in the variation of Eq.(32) we obtain (after replacing the primed indices with unprimed ones) the contribution

$$t_0 \left(1 + \frac{x_0}{2}\right) \rho(\alpha\beta\gamma) \psi_\lambda(\alpha\beta\gamma) , \quad (33)$$

where we have rewritten a summation as the total density. The same procedure can be carried out for the nonlocal terms in the energy density. A typical term is illustrated below

$$\begin{aligned} (\nabla \psi_\lambda^\pm)_{\alpha\beta\gamma} &= \sum_{\alpha'} D_{\alpha'}^{\alpha'} \psi_\lambda^\pm(\alpha'\beta\gamma) \hat{i} + \sum_{\beta'} D_{\beta'}^{\beta'} \psi_\lambda^\pm(\alpha\beta'\gamma) \hat{j} \\ &+ \sum_{\gamma'} D_{\gamma'}^{\gamma'} \psi_\lambda^\pm(\alpha\beta\gamma') \hat{k} \end{aligned}$$

where the matrices \mathbf{D} denote the first derivative matrices in x, y, z directions (they can be different although the notation does not make this obvious), calculated as described in the previous section. Finally, the HF equations can be written as matrix-vector equations on the collocation lattice

$$h\psi_\lambda^\pm \longrightarrow \mathbf{h} \cdot \psi_\lambda^\pm . \quad (34)$$

The essence of this construction is that the terms in the single-particle Hamiltonian \mathbf{h} are matrices in one coordinate and diagonal in others. Therefore, \mathbf{h} need not be stored as a full matrix, which allows the handling of very large systems directly in memory. The details of this procedure are discussed below.

3.4 Solution of the discrete equations

In this subsection we will outline some of the numerical methods developed for the solution of the discretized HF and TDHF equations. The subsection is divided into two parts; the first part discusses the static iteration methods and the solution of the field equations and in particular the powerful damped relaxation method [55]. In addition we discuss the implementation of external constraints on the HF equations. The second part of the subsection introduces a number of time-evolution methods used in our calculations. Typical numerical accuracies are also discussed.

3.4.1 Static solutions

The solution of the HF equations (34) represent the problem of finding the few lowest eigenvalues of a very large Hamiltonian matrix. Furthermore, due to the fact that we are dealing with a self-consistent problem the matrix elements must be recalculated at every iteration. However, in practice the matrix elements need not be stored. Instead, one can make use of the inherent sparsity to dynamically construct the operation of the single-particle Hamiltonian onto a statevector. The basic operation is

$$\psi' = \mathbf{h} \cdot \psi , \quad (35)$$

where the construction of the right hand side is done by explicitly programming the required linear combinations of the elements of ψ to give ψ' . In this approach the only storage requirements are for the statevectors and small matrices present in the Hamiltonian.

The lattice equations are solved by using the damped relaxation method described in Refs. [29, 55]. A simple way for introducing the damped relaxation method is by pointing out its resemblance to the so-called imaginary time method. A more formal discussion is given

in Ref. [55] where the generalization to the relativistic Dirac equation is also introduced. We start with the TDHF equations

$$i\hbar \frac{\partial \psi_\lambda}{\partial t} = \mathbf{h}(t)\psi_\lambda. \quad (36)$$

In terms of the discretized time $t_n = n\Delta t$ the solution at time $n + 1$ can be obtained from time n by (see below)

$$\psi_\lambda^{n+1} = e^{-i\Delta t \mathbf{h}^n / \hbar} \psi_\lambda^n, \quad (37)$$

where \mathbf{h}^n is the single-particle Hamiltonian at the n^{th} iteration. The imaginary time-step method consists of the transformation $\Delta t \rightarrow -i\Delta t$

$$\chi_\lambda^{n+1} = e^{-x_0(\mathbf{h}^n - \epsilon_\lambda^n)} \chi_\lambda^n, \quad (38)$$

where $x_0 = \Delta t / \hbar$, and we have taken out a trivial phase from ψ_λ^n . The expansion of the exponential to first order in x_0 yields the imaginary time iteration scheme

$$\chi_\lambda^{n+1} = \mathcal{O}[\chi_\lambda^n - x_0(\mathbf{h}^n - \epsilon_\lambda^n)\chi_\lambda^n], \quad (39)$$

where \mathcal{O} stands for Gram-Schmidt orthonormalization, which is necessary to ensure the orthonormality of the single-particle states at each iteration. In Eq. (39) the index n is no longer associated with time and it simply becomes an iteration counter. It is clear from Eq. (38) that the exponential acts as a filter in selecting the lowest eigenvalues of \mathbf{h} and leads to the minimization of the HF energy. The generalization of the imaginary time method, where we introduce the damping matrix \mathbf{D} , results in the damped relaxation method

$$\chi_\lambda^{n+1} = \mathcal{O}[\chi_\lambda^n - x_0 \mathbf{D}(E_0)(\mathbf{h}^n - \epsilon_\lambda^n)\chi_\lambda^n]. \quad (40)$$

The damping operator \mathbf{D} is chosen to be

$$\begin{aligned} \mathbf{D}(E_0) &= \left[1 + \frac{\mathbf{T}}{E_0} \right]^{-1} \\ &\approx \left[1 + \frac{\mathbf{T}_x}{E_0} \right]^{-1} \left[1 + \frac{\mathbf{T}_y}{E_0} \right]^{-1} \left[1 + \frac{\mathbf{T}_z}{E_0} \right]^{-1}, \end{aligned}$$

where \mathbf{T} denotes the kinetic energy operator. Limits can be established for the ranges of the parameters x_0 and E_0 [55], but in practice fine-tuning is necessary for optimal performance. Two convergence criteria are used in practical calculations; one being the fractional change in the HF energy

$$\Delta E^n = \frac{E^{n+1} - E^n}{E^n}, \quad (41)$$

and other the fluctuations in energy

$$\eta \equiv \sqrt{\langle H^2 \rangle - \langle H \rangle^2}. \quad (42)$$

The fluctuations are a more stringent condition than the simple energy difference between two iterations. In practice, we have required η to be less than 10^{-6} . For this value of the energy fluctuation the fractional change in the HF energy is about 10^{-13} .

The calculation of the HF Hamiltonian also requires the evaluation of the direct Coulomb contribution. However, since the calculation of the three-dimensional Coulomb integral is very costly, we solve instead the corresponding differential equation

$$\nabla^2 U_C(\mathbf{r}) = -4\pi e^2 \rho_p(\mathbf{r}). \quad (43)$$

Details of solving the Poisson equation using the BSCM is given in Ref. [51].

3.4.2 Constrained HF calculations

It is sometimes desirable to solve the static HF equations away from the global minimum in energy. Such situations usually arise in the study of fission barriers and in the study of long-lived superdeformed states of nuclei that can be formed during low energy heavy-ion collisions. These methods have been instrumental for the understanding of the formation of nuclear molecules [29]. All of these cases require the existence of a stable minimum which does not coincide with the ground state configuration. The usual approach is to study the HF energy of a nuclear system by keeping certain macroscopic degrees of freedom at pre-specified values. This results in a multi-dimensional *energy surface* from which extremum values can be obtained. The reliability of these results depend strongly on the correct identification of the relevant macroscopic degrees of freedom. However, as we will see below a special constrained HF method, *density constrained HF*, has also been developed which allows the minimization of the energy along a TDHF trajectory.

The goal is to devise an iteration scheme such that the expectation value of an arbitrary operator \hat{Q} does not change from one static iteration to next

$$\sum_{\lambda} \langle \chi_{\lambda}^{n+1} | \hat{Q} | \chi_{\lambda}^{n+1} \rangle = \sum_{\lambda} \langle \chi_{\lambda}^n | \hat{Q} | \chi_{\lambda}^n \rangle . \quad (44)$$

Furthermore, we require this expectation value to be a fixed number Q_0 . A procedure can be developed by using Lagrange multipliers that are dynamically adjusted [29]. We start with the static HF iteration scheme modified by the addition of a constraint (we have omitted the damping matrix \mathbf{D} in the equations below for simplicity)

$$\chi_{\lambda}^{n+1} = \mathcal{O}[\chi_{\lambda}^n - x_0(\mathbf{h}^n + \lambda \hat{Q} - \epsilon_{\lambda}^n) \chi_{\lambda}^n] . \quad (45)$$

In Ref.[29] we give a set of exact equations which preserve the expectation of the constraining operator to order x_0^2 . However, these equations involve the calculation of exchange terms and may become costly. Instead, one can develop a simpler iterative scheme as follows. Perform an intermediate step

$$\chi_{\lambda}^{n+1/2} = \mathcal{O}[\chi_{\lambda}^n - x_0(\mathbf{h}^n + \lambda^n \hat{Q} - \epsilon_{\lambda}^n) \chi_{\lambda}^n] , \quad (46)$$

and calculate the difference

$$\delta Q^{n+1/2} = \sum_{\lambda} \langle \chi_{\lambda}^{n+1/2} | \hat{Q} | \chi_{\lambda}^{n+1/2} \rangle - \sum_{\lambda} \langle \chi_{\lambda}^n | \hat{Q} | \chi_{\lambda}^n \rangle . \quad (47)$$

In analogy with the exact case the Lagrange parameter λ is altered to reduce this difference

$$\lambda^{n+1} = \lambda^n + c_0 \frac{\delta Q^{n+1/2}}{2x_0 \sum_{\lambda} \langle \chi_{\lambda}^n | \hat{Q}^2 | \chi_{\lambda}^n \rangle + d_0} , \quad (48)$$

where c_0 and d_0 are empirical parameters replacing the exchange terms. In terms of these intermediate states the $(n+1)$ st step is given by

$$\chi_{\lambda}^{n+1} = \mathcal{O}[\chi_{\lambda}^{n+1/2} - x_0(\lambda^{n+1} - \lambda^n + \delta \lambda^n) \hat{Q} \chi_{\lambda}^{n+1/2}] , \quad (49)$$

where

$$\delta \lambda^n = \frac{\sum_{\lambda} \langle \chi_{\lambda}^n | \hat{Q} | \chi_{\lambda}^n \rangle - Q_0}{2x_0 \sum_{\lambda} \langle \chi_{\lambda}^n | \hat{Q}^2 | \chi_{\lambda}^n \rangle + d_0} . \quad (50)$$

The extension of the method which allows the entire density to be constrained is straightforward. In this case we would like to constrain a continuous density

$$\rho^n(\mathbf{r}) = \sum_{\lambda} |\chi_{\lambda}^n(\mathbf{r})|^2 , \quad (51)$$

to be equal to $\rho_0(\mathbf{r})$. The constraining operator \hat{Q} becomes the density operator $\hat{\rho}(\mathbf{r})$ defined in the single-particle space

$$\langle \chi_{\lambda}^n | \hat{\rho}(\mathbf{r}) | \chi_{\lambda}^n \rangle = |\chi_{\lambda}^n(\mathbf{r})|^2 \quad (52)$$

and the product $\lambda\hat{Q}$ is replaced by an integral

$$\lambda\hat{Q} \longrightarrow \int d^3r \lambda(\mathbf{r})\hat{\rho}(\mathbf{r}) = \lambda(\mathbf{r}) . \quad (53)$$

The last equality is due to the fact that in coordinate space $\hat{\rho}(\mathbf{r})$ is a delta function. An iterative scheme for $\lambda^n(\mathbf{r})$ is given by

$$\lambda^{n+1}(\mathbf{r}) = \lambda^n(\mathbf{r}) + c_0 \frac{\delta\rho^{n+1/2}}{2x_0\rho^n(\mathbf{r}) + d_0} , \quad (54)$$

where

$$\delta\rho^{n+1/2}(\mathbf{r}) \equiv \rho^{n+1/2}(\mathbf{r}) - \rho_0(\mathbf{r}) \quad (55)$$

is obtained from half-time iteration step

$$\chi_\lambda^{n+1/2} = \mathcal{O}[\chi_\lambda^n - x_0(\mathbf{h}^n + \lambda^n(\mathbf{r}) - \epsilon_\lambda^n)\chi_\lambda^n] . \quad (56)$$

Note that in these equations we require that the density remain equal to $\rho_0(\mathbf{r})$ at every iteration and not just at the final step. Using these wavefunctions the full iteration can be written as

$$\chi_\lambda^{n+1} = \mathcal{O}[\chi_\lambda^{n+1/2} - x_0(\lambda^{n+1}(\mathbf{r}) - \lambda^n(\mathbf{r}) + \delta\lambda^n(\mathbf{r}))\chi_\lambda^{n+1/2}] , \quad (57)$$

where

$$\delta\lambda^n(\mathbf{r}) = c_0 \frac{\rho^n(\mathbf{r}) - \rho_0(\mathbf{r})}{2x_0\rho_0(\mathbf{r}) + d_0} . \quad (58)$$

During the density constrained HF iterations the single-particle states readjust to minimize the energy while the initial density is kept fixed. In practical calculations the parameter x_0 has been replaced by the damping operator and the constants c_0 and d_0 were chosen to be 1.9 and 5×10^{-5} , respectively.

3.4.3 Time evolution

The formal solution of the TDHF equations (5) is

$$\psi_\lambda(t) = U(t, t_0)\psi_\lambda(t_0) , \quad (59)$$

where we have omitted the spatial coordinates for simplicity and the time propagator $U(t, t_0)$ is given by

$$U(t, t_0) = \mathcal{T} \exp \left[\frac{-i}{\hbar} \int_{t_0}^t dt' h(t') \right] . \quad (60)$$

The quantity \mathcal{T} denotes time-ordering which is necessary in the general case. In practical calculations we discretize time as

$$t_n = n\Delta t \quad n = 0, 1, 2, \dots, N , \quad (61)$$

and express the evolution operator in successive infinitesimal pieces

$$U(t, t_0) = U(t, t_{N-1})U(t_{N-1}, t_{N-2})\dots U(t_1, t_0) . \quad (62)$$

In this case the time-ordering operator can be ignored. For three-dimensional calculations the exponential operator is expanded as a Taylor series

$$U(t_{n+1}, t_n) \approx \left(1 + \sum_{k=1}^K \frac{(-i\Delta t \mathbf{h}/\hbar)^k}{k!} \right) . \quad (63)$$

The expansion of the operator requires repeated applications of \mathbf{h} onto the wavefunctions. In practice, only 6–8 terms are needed for the conservation of the norm at 1 part in 10^{-10} level during the entire time-evolution. The expansion method is also attractive due to the fact that it only involves matrix vector operations which could be easily customized for vector or parallel computers.

4 Numerical results

4.1 Fusion Calculations for Neutron-Rich and Stable Nuclei

In fusion experiments with neutron-rich radioactive ion beams, the dynamics of the neutron skin usually enhances the sub-barrier fusion cross section over that predicted by a simple static barrier penetration model, but in some cases suppression of fusion is also observed. Most recently, we have investigated sub-barrier fusion and pre-equilibrium giant resonance excitation between various tin + calcium isotopes [56, 57] and calcium + calcium isotopes [20]. Finally, we have studied sub-barrier fusion reactions between both stable and neutron-rich isotopes of oxygen and carbon [58–60] that occur in the neutron star crust. In all cases, we have found good agreement between the measured fusion cross sections and the DC-TDHF results. This is rather remarkable given the fact that the only input in DC-TDHF is the Skyrme effective N-N interaction, and there are no adjustable parameters.

In several experiments, large enhancements of sub-barrier fusion yields have been observed for systems with positive Q values for neutron transfer. Recently, a series of experiments has been carried out with radioactive ^{132}Sn beams and with stable ^{124}Sn beams on $^{40,48}\text{Ca}$ targets [61]. It turns out that the $^{40}\text{Ca}+\text{Sn}$ systems have many positive Q values for neutron-pickup while all the Q values for $^{48}\text{Ca}+\text{Sn}$ are negative. However, the data analysis reveals that the fusion enhancement is not proportional to the magnitudes of those Q values.

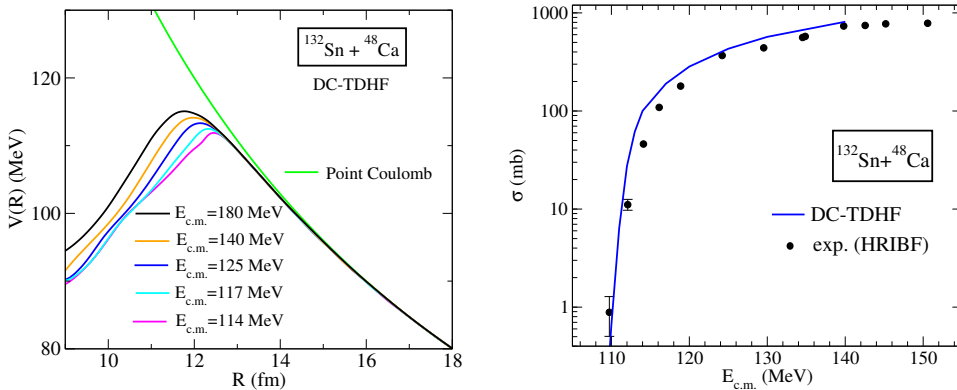


Figure 2: Left: DC-TDHF calculation [56, 57] of heavy-ion interaction potentials for the neutron-rich system $^{132}\text{Sn}+^{48}\text{Ca}$. The potentials are shown at five $E_{c.m.}$ energies. Right: Total fusion cross section as a function of center-of-mass energy. The experimental data are taken from Ref. [61].

First, we consider the neutron-rich system $^{132}\text{Sn}+^{48}\text{Ca}$. Results for the heavy-ion interaction potential $V(R)$ with the DC-TDHF method [56, 57] are shown in Fig. 2 on the left side. In general, the ion-ion potentials are energy-dependent, and they are shown here at five $E_{c.m.}$ energies. Our results demonstrate that in these heavy systems the potential barrier height increases dramatically with increasing energy, and the barrier peak moves inward towards smaller R -values. On the right side of Fig. 2 we show the calculated fusion cross section as a function of $E_{c.m.}$. In this case, we have used the theoretical cross sections obtained with the energy-dependent DC-TDHF potentials [56]. We can see that our theoretical cross sections agree remarkably well with the experimental data.

Particularly puzzling is the experimental observation of a sub-barrier fusion enhancement in the system $^{132}\text{Sn}+^{40}\text{Ca}$ as compared to more neutron-rich system $^{132}\text{Sn}+^{48}\text{Ca}$. This is difficult to understand because the 8 additional neutrons in ^{48}Ca should increase the attractive strong nuclear interaction and thus lower the fusion barrier, resulting in an enhanced sub-barrier fusion cross section. But the opposite is found experimentally. A coupled channel analysis [61] of the fusion data with phenomenological heavy-ion potentials yields cross sections that are one order of magnitude too small at sub-barrier energies, despite the fact that these ion-ion potentials contain many adjustable parameters. Using the microscopic DC-TDHF approach we are able to explain the measured sub-barrier fusion en-

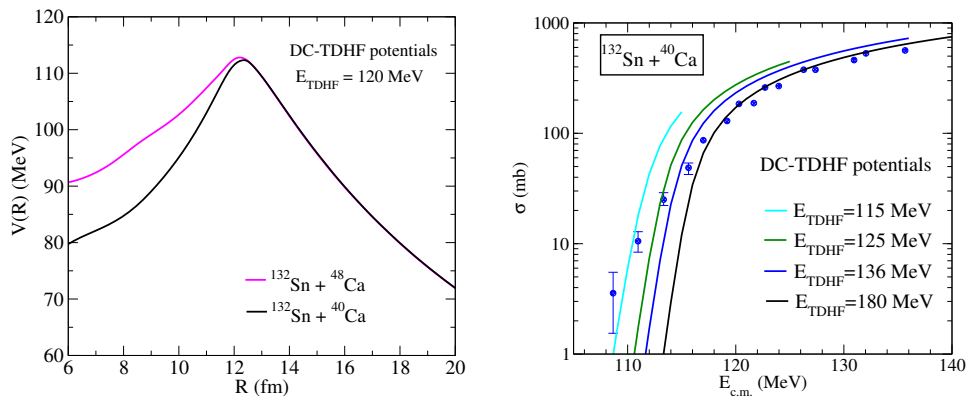


Figure 3: Left: Comparison of DC-TDHF heavy-ion interaction potentials, calculated at $E_{c.m.} = 120$ MeV, for the systems $^{132}\text{Sn}+^{40}\text{Ca}$ and $^{132}\text{Sn}+^{48}\text{Ca}$. Right: Total fusion cross sections for $^{132}\text{Sn}+^{40}\text{Ca}$ as a function of center-of-mass energy. The cross sections have been calculated for several energy-dependent potentials. The experimental data are taken from Ref. [61].

hancement [57] in terms of the *narrower width* of the ion-ion potential for $^{132}\text{Sn}+^{40}\text{Ca}$, while the barrier heights and positions are approximately the same in both systems, see Fig. 3. The energy-dependence of the heavy-ion interaction potentials is crucial for understanding the low-energy fusion data.

As another example, we discuss our theoretical analysis of recent $^{40,48}\text{Ca} + ^{40,48}\text{Ca}$ fusion data [62] which extend older fusion data to low sub-barrier energies. Comparison of the sub-barrier cross sections with those calculated using standard coupled-channel calculations suggested a hindrance of the fusion cross-sections at deep sub-barrier energies. The DC-TDHF results for the ion-ion potentials and fusion cross section [20] are shown in Fig. 4. In contrast to the heavy systems discussed above, we find that the ion-ion potentials for

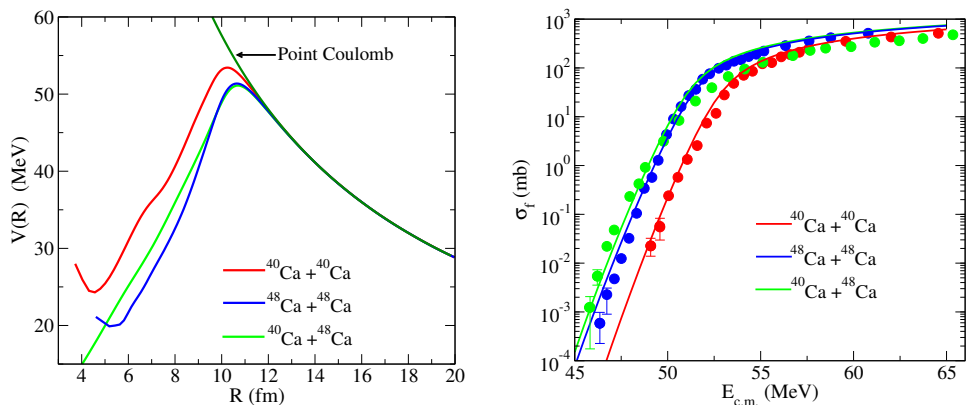


Figure 4: DC-TDHF ion-ion potentials (left) and fusion cross-sections (right) for various isotopes of the Ca+Ca system [20]. The experimental data are taken from Ref. [62].

lighter systems depend only weakly on the energy, and the potential barrier corresponding to the lowest collision energy gives the best fit to the sub-barrier cross-sections since this is the one that allows for more rearrangements to take place and grows the inner part of the barrier. Considering the fact that historically the low-energy sub-barrier cross-sections of the $^{40}\text{Ca}+^{48}\text{Ca}$ system have been the ones not reproduced well by the standard models, the DC-TDHF results are quite satisfactory, indicating that the dynamical evolution of the nuclear density in TDHF gives a good overall description of the collision process.

Figure 5 shows the excitation energy, $E^*(R)$, for the three systems studies here. The excitation energy was calculated for the same value of $\varepsilon = E_{c.m.}/\mu = 2.75$ MeV for all systems, which corresponds to collision energies of 55, 60, and 66 MeV, respectively. All

curves initially behave in a similar manner, at large distances the excitation is zero, as the nuclei approach the barrier peak the excitations start and monotonically rise for larger overlaps. The interesting observation is that the excitations for the intermediary $^{40}\text{Ca}+^{48}\text{Ca}$ system start at a slightly earlier time and rise above the other two systems. This may be largely due to the fact that an asymmetric system has some additional modes of excitation in comparison to the other two symmetric systems.

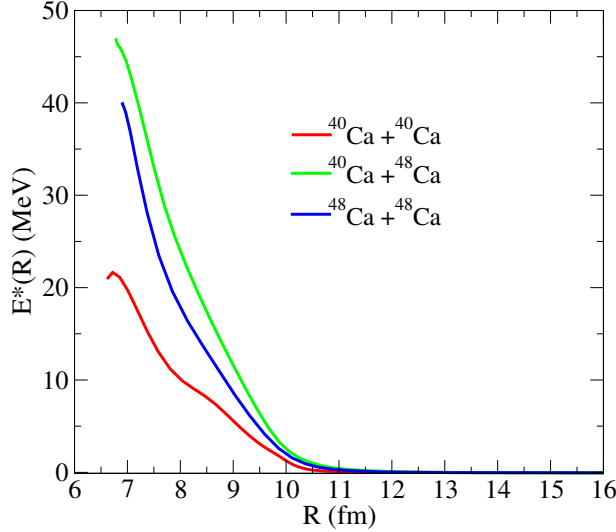


Figure 5: Excitation energy $E^*(R)$, for three isotopic combinations of the Ca+Ca system [20].

4.2 Hot and Cold Fusion to Produce Superheavy Elements

In connection with superheavy element production, we have studied the hot fusion reaction $^{48}\text{Ca}+^{238}\text{U}$ and the cold fusion reaction $^{70}\text{Zn}+^{208}\text{Pb}$ [18]. Considering hot fusion, ^{48}Ca is a spherical nucleus whereas ^{238}U has a large axial deformation. The deformation of ^{238}U strongly influences the interaction barrier for this system. This is shown in Fig. 6, which shows the interaction barriers, $V(R)$, calculated using the DC-TDHF method as a function of c.m. energy and for three different orientations of the ^{238}U nucleus. The alignment angle β is the angle between the symmetry axis of the ^{238}U nucleus and the collision axis.

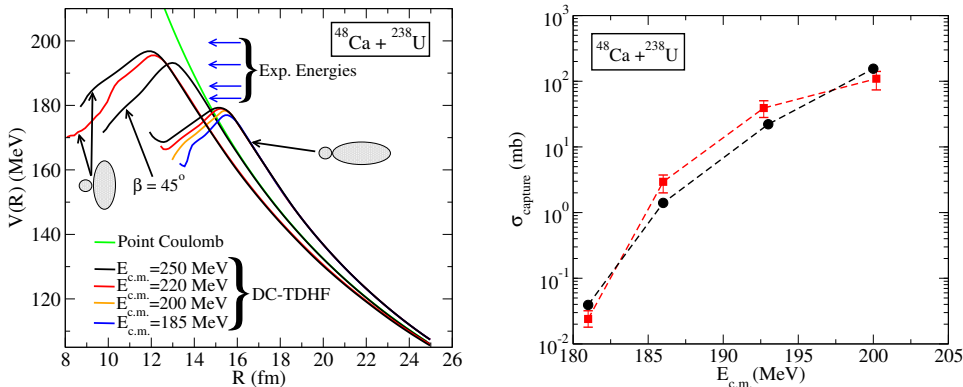


Figure 6: Left: Potential barriers, $V(R)$, obtained from DC-TDHF calculations [18] as a function of $E_{c.m.}$ energy and orientation angle β of the ^{238}U nucleus. Also shown are the experimental c.m. energies. Right: Capture cross-sections as a function of $E_{c.m.}$ energy (black circles). Also shown are the experimental cross-sections [63, 64] (red squares).

The barriers for the polar orientation ($\beta = 0^\circ$) of the ^{238}U nucleus are much lower and peak at larger ion-ion separation distance R . On the other hand, the barriers for the equatorial orientation ($\beta = 90^\circ$) are higher and peak at smaller R values. We observe that at lower energies the polar orientation results in sticking of the two nuclei, while the equatorial orientation results in a deep-inelastic collision. We have also calculated the excitation energy $E^*(R)$ as a function of c.m. energy and orientation angle β of the ^{238}U nucleus. The system is excited much earlier during the collision process for the polar orientation and has a higher excitation than the corresponding collision for the equatorial orientation.

To obtain the capture cross-section, we calculate potential barriers $V(R, \beta)$ for a set of initial orientations β of the ^{238}U nucleus. Then we determine partial cross sections $\sigma(\beta)$ and perform an angle-average, including the dynamic alignment arising from Coulomb excitation of the g.s. rotational band in the entrance channel. In Fig. 6 we show our results for the capture cross-sections which are in remarkably good agreement with experimental data.

One of the major questions that is asked by the experimental superheavy element community is why a ^{48}Ca beam is so crucial in forming such systems and whether one could produce new superheavy nuclei using projectiles different than ^{48}Ca and actinide targets. Some possible projectiles include ^{50}Ti , ^{54}Cr , ^{56}Fe and ^{64}Ni . Several reactions with these projectiles were tried, no SHE event reported so far, only cross section limits. Typical reactions studied already are $^{238}\text{U} + ^{64}\text{Ni}$ (SHIP GSI), $^{248}\text{Cm} + ^{54}\text{Cr}$ (SHIP) and $^{248}\text{Cm} + ^{56}\text{Fe}$ (Dubna), $^{50}\text{Ti} + ^{249}\text{Bk}$ and $^{50}\text{Ti} + ^{249}\text{Cf}$ (TASCA GSI). During the ICFN5 meeting at Sanibel Island, Florida a particularly low cross section limit, of about 50 fb, was reported for the production of isotopes of new element 119 in the reaction between ^{50}Ti and ^{249}Bk . The reaction $^{48}\text{Ca} + ^{249}\text{Bk}$ makes superheavy isotopes of element 117 with cross-sections of 2 – 3 picobarns, by contrast the $^{50}\text{Ti} + ^{249}\text{Bk}$ reaction yields a cross-section limit of 50 fb, about 50 times lower. TDHF can be used to calculate capture cross-sections, excitation energies, and other dynamical properties for some of these systems in order to find the discerning physical property among them.

4.3 Nuclear Astrophysics: Fusion of Oxygen and Carbon in the Neutron Star Crust

Fusion of very neutron rich nuclei may be important to determine the composition and heating of the crust of accreting neutron stars. We have studied sub-barrier fusion reactions between both stable and neutron-rich isotopes of oxygen and carbon. In Fig. 7 (left side) we show the DC-TDHF potential barriers for the C+O system [58]. The higher barrier corresponds to the $^{12}\text{C} + ^{16}\text{O}$ system and has a peak energy of 7.77 MeV. The barrier for the $^{12}\text{C} + ^{24}\text{O}$ system occurs at a slightly larger R value with a barrier peak of 6.64 MeV. The right side of Fig. 7 shows the corresponding cross sections for the two reactions. Also shown are the experimental data from Ref. [65]. The DC-TDHF potential reproduces the experimental cross-sections quite well for the $^{12}\text{C} + ^{16}\text{O}$ system, and the cross section for the neutron rich $^{12}\text{C} + ^{24}\text{O}$ is predicted to be larger than that for $^{12}\text{C} + ^{16}\text{O}$. Similar agreement with fusion data for the $^{16}\text{O} + ^{16}\text{O}$ system and the predicted cross-sections for heavier oxygen isotopes were also calculated [58].

Summary

In this manuscript we have outlined the microscopic study of fusion using the DC-TDHF approach. For a variety of heavy-ion reactions, we discuss the results of our numerical calculations of fusion / capture cross-sections at energies below and above the Coulomb barrier and compare these to experimental data if available. In this context we discuss a variety of stable and neutron-rich reaction partners, and we examine hot fusion reactions leading to the formation of superheavy elements. Fusion of very neutron rich light nuclei also plays a major role in nuclear astrophysics where it determines the composition and heating of the crust of accreting neutron stars. We have shown that microscopically obtained ion-ion potentials do give a reasonably good description of these fusion cross-sections.

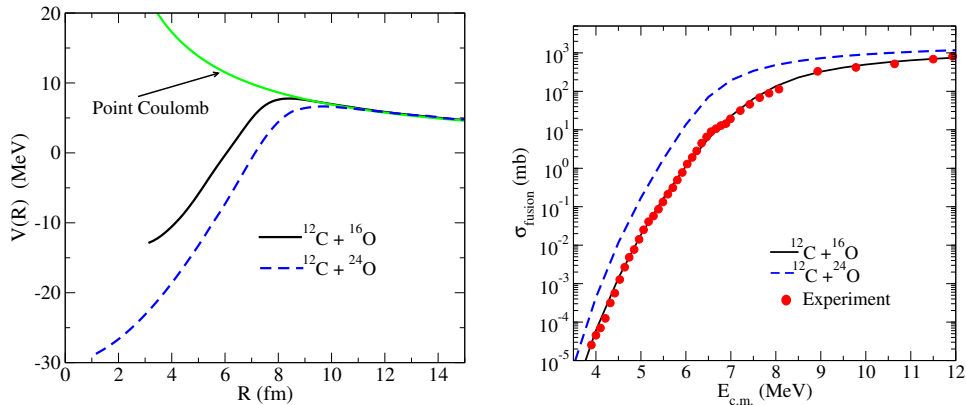


Figure 7: Left: DC-TDHF heavy-ion potentials for the systems $^{12}\text{C}+^{16,24}\text{O}$. Right: Total fusion cross sections versus center-of-mass energy for fusion of carbon with oxygen isotopes [58]. The experimental data are from Ref. [65].

The fully microscopic TDHF theory has shown itself to be rich in nuclear phenomena and continues to stimulate our understanding of nuclear dynamics. The time-dependent mean-field studies seem to show that the dynamic evolution builds up correlations that are not present in the static theory. While modern Skyrme forces provide a much better description of static nuclear properties in comparison to the earlier parametrizations there is a need to obtain even better parametrizations that incorporate deformation and reaction data into the fit process.

Acknowledgment

We would like to extend our best wishes to Prof. Joachim Maruhn for his retirement. Since the 1970's Prof. Maruhn has made significant contributions to the development of time-dependent mean-field theories and lead the way for the new generation of nuclear physicists to build upon this foundation. Both as a colleague and a friend we would like to extend our gratitude to him. This work has been supported by the U.S. Department of Energy under grant No. DE-FG02-96ER40975 with Vanderbilt University.

References

- [1] A. B. Balantekin, J. Carlson, D. J. Dean, G. M. Fuller, R. J. Furnstahl, M. Hjorth-Jensen, R. V. F. Janssens, B.-A. Li, W. Nazarewicz, F. M. Nunes, W. E. Ormand, S. Reddy, and B. M. Sherrill, *Mod. Phys. Lett. A* **29**, 1430010 (2014).
- [2] B. B. Back, H. Esbensen, C. L. Jiang, and K. E. Rehm, *Rev. Mod. Phys.* **86**, 317 (2014).
- [3] S. Mişicu and H. Esbensen, *Phys. Rev. Lett.* **96**, 112701 (2006).
- [4] Kouichi Hagino and Noboru Takigawa, *Prog. Theo. Phys.* **128**, 1001 (2012).
- [5] C. Simenel, M. Dasgupta, D. J. Hinde, and E. Williams, *Phys. Rev. C* **88**, 064604 (2013).
- [6] Kouhei Washiyama and Denis Lacroix, *Phys. Rev. C* **78**, 024610 (2008).
- [7] A. S. Umar, C. Simenel, and V. E. Oberacker, *Phys. Rev. C* **89**, 034611 (2014).
- [8] X. Jiang, J. A. Maruhn, and S. Yan, *Phys. Rev. C* **90**, 064618 (2014).

- [9] L. C. Chamon, B. V. Carlson, L. R. Gasques, D. Pereira, C. De Conti, M. A. G. Alvarez, M. S. Hussein, M. A. C. Ribeiro, E. S. Rossi, and C. P. Silva, *Phys. Rev. C* **66**, 014610 (2002).
- [10] A. S. Umar and V. E. Oberacker, *Phys. Rev. C* **74**, 021601 (2006).
- [11] A. S. Umar, V. E. Oberacker, J. A. Maruhn, and P.-G. Reinhard, *Phys. Rev. C* **80**, 041601 (2009).
- [12] R. Y. Cusson, P.-G. Reinhard, M. R. Strayer, J. A. Maruhn, and W. Greiner, *Z. Phys. A* **320**, 475 (1985).
- [13] A. S. Umar and V. E. Oberacker, *Phys. Rev. C* **74**, 024606 (2006).
- [14] A. S. Umar and V. E. Oberacker, *Phys. Rev. C* **74**, 061601 (2006).
- [15] A. S. Umar and V. E. Oberacker, *Phys. Rev. C* **76**, 014614 (2007).
- [16] A. S. Umar and V. E. Oberacker, *Phys. Rev. C* **77**, 064605 (2008).
- [17] A. S. Umar and V. E. Oberacker, *Eur. Phys. J. A* **39**, 243 (2009).
- [18] A. S. Umar, V. E. Oberacker, J. A. Maruhn, and P.-G. Reinhard, *Phys. Rev. C* **81**, 064607 (2010).
- [19] V. E. Oberacker, A. S. Umar, J. A. Maruhn, and P.-G. Reinhard, *Phys. Rev. C* **82**, 034603 (2010).
- [20] R. Keser, A. S. Umar, and V. E. Oberacker, *Phys. Rev. C* **85**, 044606 (2012).
- [21] C. Simenel, R. Keser, A. S. Umar, and V. E. Oberacker, *Phys. Rev. C* **88**, 024617 (2013).
- [22] C. Simenel and P. Chomaz, *Phys. Rev. C* **68**, 024302 (2003).
- [23] T. Nakatsukasa and K. Yabana, *Phys. Rev. C* **71**, 024301 (2005).
- [24] A. S. Umar and V. E. Oberacker, *Phys. Rev. C* **71**, 034314 (2005).
- [25] J. A. Maruhn, P. G. Reinhard, P. D. Stevenson, J. Rikovska Stone, and M. R. Strayer, *Phys. Rev. C* **71**, 064328 (2005).
- [26] J. W. Negele, *Rev. Mod. Phys.* **54**, 913 (1982).
- [27] C. Simenel, *Eur. Phys. J. A* **48**, 152 (2012).
- [28] A. S. Umar and V. E. Oberacker, *J. Phys. G* **36**, 025101 (2009).
- [29] A. S. Umar, M. R. Strayer, R. Y. Cusson, P.-G. Reinhard, and D. A. Bromley, *Phys. Rev. C* **32**, 172 (1985).
- [30] A. S. Umar, V. E. Oberacker, and J. A. Maruhn, *Eur. Phys. J. A* **37**, 245 (2008).
- [31] C. Simenel, *Phys. Rev. Lett.* **105**, 192701 (2010).
- [32] Kazuyuki Sekizawa and Kazuhiro Yabana, *Phys. Rev. C* **88**, 014614 (2013).
- [33] K. Goeke, F. Grümmer, and P.-G. Reinhard, *Ann. Phys.* **150**, 504 (1983).
- [34] G. H. Rawitscher, *Phys. Rev.* **135**, B605 (1964).
- [35] K. Hagino, N. Rowley, and A. T. Kruppa, *Comput. Phys. Commun.* **123**, 143 (1999).
- [36] A. S. Umar, M. R. Strayer, and P.-G. Reinhard, *Phys. Rev. Lett.* **56**, 2793 (1986).

- [37] P.-G. Reinhard, A. S. Umar, K. T. R. Davies, M. R. Strayer, and S. J. Lee, Phys. Rev. C **37**, 1026 (1988).
- [38] A. S. Umar, M. R. Strayer, P.-G. Reinhard, K. T. R. Davies, and S.-J. Lee, Phys. Rev. C **40**, 706 (1989).
- [39] A. S. Umar and V. E. Oberacker, Phys. Rev. C **73**, 054607 (2006).
- [40] E. B. Suckling and P. D. Stevenson, EPL **90**, 12001 (2010).
- [41] S. Fracasso, E. B. Suckling, and P. D. Stevenson, Phys. Rev. C **86**, 044303 (2012).
- [42] M. Tohyama and A. S. Umar, Phys. Lett. B **549**, 72 (2002).
- [43] M. Tohyama and A. S. Umar, Phys. Rev. C **65**, 037601 (2002).
- [44] Shuichiro Ebata, Takashi Nakatsukasa, Tsunenori Inakura, Kenichi Yoshida, Yukio Hashimoto, and Kazuhiro Yabana, Phys. Rev. C **82**, 034306 (2010).
- [45] J. A. Maruhn, P.-G. Reinhard, P. D. Stevenson, and A. S. Umar, Comp. Phys. Comm. **185**, 2195 (2014).
- [46] L. Guo, J. A. Maruhn, P.-G. Reinhard, and Y. Hashimoto, Phys. Rev. C **77**, 041301 (2008).
- [47] E. Chabanat, P. Bonche, P. Haensel, J. Meyer, and R. Schaeffer, Nucl. Phys. A **635**, 231 (1998).
- [48] P. Klüepfel, P.-G. Reinhard, T. J. Bürvenich, and J. A. Maruhn, Phys. Rev. C **79**, 034310 (2009).
- [49] M. Kortelainen, T. Lesinski, J. More, W. Nazarewicz, J. Sarich, N. Schunck, M. V. Stoitsov, and S. Wild, Phys. Rev. C **82**, 024313 (2010).
- [50] M. Kortelainen, J. McDonnell, W. Nazarewicz, P.-G. Reinhard, J. Sarich, N. Schunck, M. V. Stoitsov, and S. M. Wild, Phys. Rev. C **85**, 024304 (2012).
- [51] A. S. Umar, J. Wu, M. R. Strayer, and C. Bottcher, J. Comp. Phys. **93**, 426 (1991).
- [52] A. S. Umar, M. R. Strayer, J. S. Wu, D. J. Dean, and M. C. Güçlü, Phys. Rev. C **44**, 2512 (1991).
- [53] S. E. Koonin, K. T. R. Davies, V. Maruhn-Rezwani, H. Feldmeier, S. J. Krieger, and J. W. Negele, Phys. Rev. C **15**, 1359 (1977).
- [54] C. de Boor, *A Practical Guide to Splines* (Springer, 1978).
- [55] C. Bottcher, M. R. Strayer, A. S. Umar, and P.-G. Reinhard, Phys. Rev. A **40**, 4182 (1989).
- [56] V. E. Oberacker, A. S. Umar, J. A. Maruhn, and P.-G. Reinhard, Phys. Rev. C **85**, 034609 (2012).
- [57] V. E. Oberacker and A. S. Umar, Phys. Rev. C **87**, 034611 (2013).
- [58] A. S. Umar, V. E. Oberacker, and C. J. Horowitz, Phys. Rev. C **85**, 055801 (2012).
- [59] R. T. deSouza, S. Hudan, V. E. Oberacker, and A. S. Umar, Phys. Rev. C **88**, 014602 (2013).
- [60] M. J. Rudolph, Z. Q. Gosser, K. Brown, S. Hudan, R. T. de Souza, A. Chbihi, B. Jacquot, M. Famiano, J. F. Liang, D. Shapira, and D. Mercier, Phys. Rev. C **85**, 024605 (2012).

- [61] J. J. Kolata, A. Roberts, A. M. Howard, D. Shapira, J. F. Liang, C. J. Gross, R. L. Varner, Z. Kohley, A. N. Villano, H. Amro, W. Loveland, and E. Chavez, *Phys. Rev. C* **85**, 054603 (2012).
- [62] G. Montagnoli, A. M. Stefanini, C. L. Jiang, H. Esbensen, L. Corradi, S. Courtin, E. Fioretto, A. Goasduff, F. Haas, A. F. Kifle, C. Michelagnoli, D. Montanari, T. Mijatović, K. E. Rehm, R. Silvestri, P. P. Singh, F. Scarlassara, S. Szilner, X. D. Tang, and C. A. Ur, *Phys. Rev. C* **85**, 024607 (2012).
- [63] M. Itkis, A. Bogachev, I. Itkis, J. Kliman, G. Knyazheva, N. Kondratiev, E. Kozulin, L. Krupa, Y. Oganessian, I. Pokrovsky, E. Prokhorova, and A. Rusanov, *Nucl. Phys. A* **787**, 150 (2007).
- [64] Y. Oganessian, *J. Phys. G* **34**, R165 (2007).
- [65] C. L. Jiang, K. E. Rehm, B. B. Back, and R. V. F. Janssens, *Phys. Rev. C* **75**, 015803 (2007).